AGU PUBLICATIONS

Tectonics

RESEARCH ARTICLE
10.1002/2015TC004097

Key Points:
- The rifted basins and thinning crust were observed in the Taiwan Strait
- A low-velocity zone beneath the Penghu Archipelago was imaged

Supporting Information:
- Supporting Information S1

Correspondence to:
H. Kuo-Chen,
kuochen@ncu.edu.tw;
kuochen.hao@gmail.com

Citation:
Chen, K.-X., H. Kuo-Chen, D. Brown, Q. Li, Z. Ye, W.-T. Liang, C.-Y. Wang, and H. Yao (2016), Three-dimensional ambient noise tomography across the Taiwan Strait: The structure of a magma-poor rifted margin, *Tectonics*, *35*, 1782–1792, doi:10.1002/2015TC004097.

Received 2 DEC 2015
Accepted 7 JUL 2016
Accepted article online 20 JUL 2016
Published online 4 AUG 2016

Three-dimensional ambient noise tomography across the Taiwan Strait: The structure of a magma-poor rifted margin

Kai-Xun Chen[1,2], Hao Kuo-Chen[1], Dennis Brown[3], Qiusheng Li[4,5], Zhuo Ye[4,5], Wen-Tzong Liang[6], Chien-Ying Wang[1], and Huajian Yao[7]

[1]Department of Earth Sciences, National Central University, Taoyuan, Taiwan, [2]Department of Geosciences, National Taiwan University, Taipei, Taiwan, [3]Institute of Earth Science "Jaume Almera", CSIC, Barcelona, Spain, [4]Institute of Geology, Chinese Academy of Geological Sciences, Beijing, China, [5]Key Laboratory of Earthprobe and Geodynamics, Beijing, China, [6]Institute of Earth Sciences, Academia Sinica, Taipei, Taiwan, [7]Laboratory of Seismology and Physics of Earth's Interior, School of Earth and Space Sciences, University of Science and Technology of China, Hefei, China

Abstract Rifting along southeastern Eurasia in the Late Cenozoic led to the formation of a magma-poor rifted margin facing the South China Sea to the southeast and the Philippine Sea to the east. Further rifting along the outer part of the margin during the middle to late Miocene was accompanied by an extensive episode of intraplate flood volcanism that formed the Penghu Archipelago. Previous geophysical studies in the area of the strait have focused primarily on the shallow structures of the rift basins and the depth to the Moho. In this study we present the regional-scale 3-D *S* wave structure of the Taiwan Strait that is derived from a joint Chinese and Taiwanese 3-D ambient noise tomography study. The *S* wave model shows a thinning of the crust beneath the rift basins where, locally, thin high-velocity layers suggest the presence of intrusive bodies. The rift basin and the foreland basin along the west coast of Taiwan are imaged as low-velocity zones with thicknesses between 5 and 10 km and extending eastward beneath the Taiwan mountain belt. In the upper 10 km of the crust, the basaltic rocks of the Penghu Archipelago are imaged as a high-velocity zone that, with depth, becomes a relatively low-velocity zone. We interpret this low-velocity zone in the lower crust and upper mantle beneath the Penghu Archipelago to image a thermal anomaly related to the still cooling magma feeding system and the melt reservoir area that fed the flood basalts at the surface.

1. Introduction

The Taiwan Strait is a shallow water (<100 m deep) part of the magma-poor southeast Eurasian margin situated between mainland China and Taiwan. It forms a tectonically stable area that is landward of the active eastern edge of the Eurasian Plate (EUP) in the tectonically complex area on and around Taiwan. Around Taiwan, the Eurasian margin that underlies the Taiwan Strait is subducting beneath the Philippine Sea Plate (PSP) along the Manila subduction zone. At the same time, the Philippine Sea Plate is subducting northward under the Eurasian plate along the Ryukyu subduction zone, and the Okinawa Trough is forming a back-arc basin that impinges on northeastern Taiwan (Figure 1) [*Suppe*, 1984; *Sibuet and Hsu*, 1997, 2004]. The Taiwan Strait is flanked to the west by the Paleozoic Wuyi-Yunkai orogen and to the southeast by the South China Sea (Figure 1a).

Despite its importance for the structural development of the Taiwan orogen [*Lin et al*., 2003; *Mouthereau and Petit*, 2003; *Teng and Lin*, 2004], the structure of the crust and upper mantle of the Eurasian margin has not been extensively studied in the Taiwan Strait. Early studies were carried out primarily for hydrocarbon exploration purposes and were therefore focused on the shallow crustal structure and sedimentary basins [e.g., *Gao and Huang*, 1994; *Lin and Watts*, 2002; *Lin et al*., 2003] (Figure 1). Studies of the deeper crust have focused exclusively on the crustal thickness and the geometry of the Moho. For example, studies of *Pn* velocity [*Huang et al*., 1998], gravity data [*Hsieh et al*., 2009], and Rayleigh wave [*Huang et al*., 2014] and *P* wave tomography [*Kuo et al*., 2015] have shown that the crustal thickness in the Taiwan Strait is around 30 ± 2 km. Nevertheless, these crustal-scale studies were not of sufficient resolution to identify features within the crust. Finally, while these previous studies identified the upper crustal structure associated with sedimentary basins and the depth to the Moho in the Taiwan Strait, there are no geophysical studies that examine the volcanic edifice of the Penghu Archipelago and its relationship to what is otherwise defined as a magma-poor rifted margin

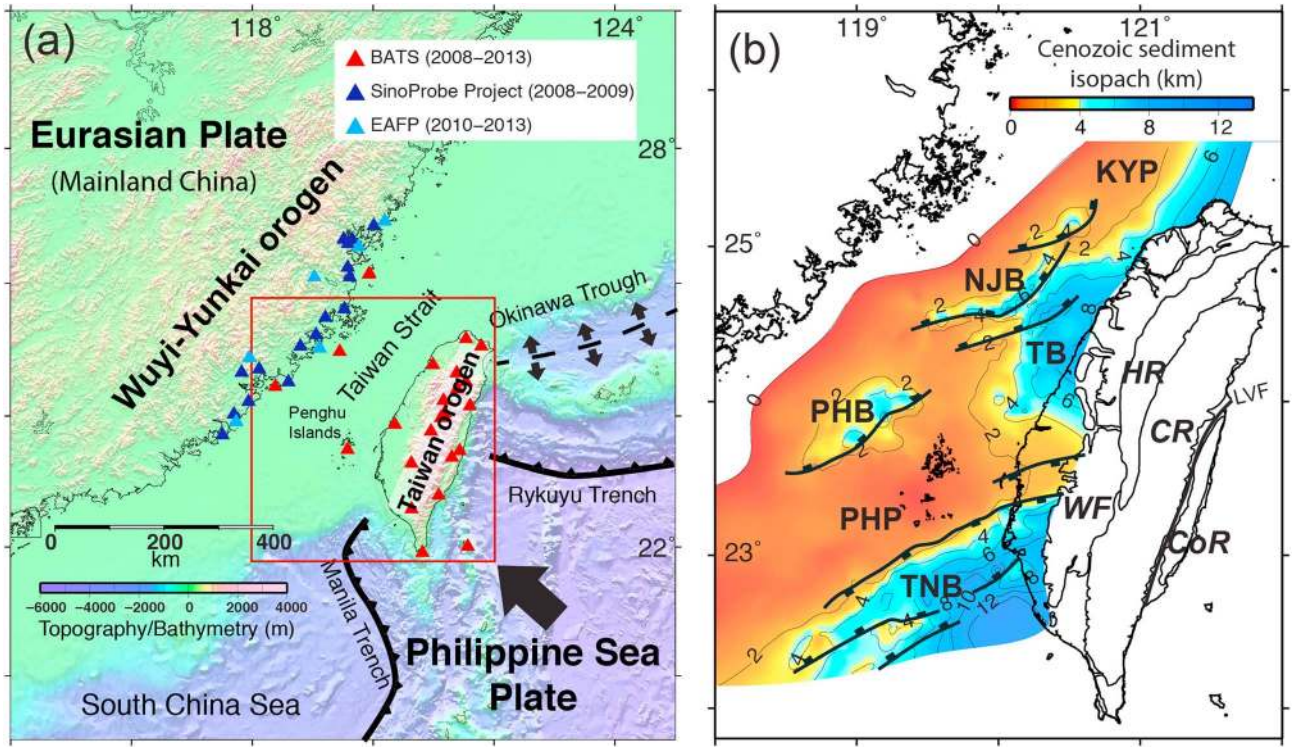

Figure 1. (a) Tectonic setting in and around the Taiwan Strait. Triangles: seismic stations. Red rectangular area: study area. BATS: broadband array in Taiwan for seismology. EAFP: Earthquake Administration of Fujian Province. (b) Cenozoic sediment isopach and normal faults geometry of Taiwan Strait [*Lin et al*., 2003]. NJB: Nanjihtao Basin. TB: Taihsi Basin. PHB: Penghu Basin. TNB: Tainan Basin. KYP: Kuanyin Platform. PHP: Penghu Platform. WF: Western Foothills. HR: H. CR: Central Range. CoR: Coastal Range. LVF: Longitudinal Valley Fault. Thick line with black solid rectangle: normal fault.

[*Yan et al*., 2006; *Franke*, 2013]. In this study, we present the results of a joint Chinese and Taiwanese study to obtain a regional-scale, 3-D *S* wave (*Vs*) model that is derived from ambient seismic noise tomography with the aim of investigating the structure of the magma-poor Eurasian continental margin beneath the Taiwan Strait.

2. Geological Background

The part of the Eurasian margin that underlies the Taiwan Strait evolved from a subcontinental subduction system in the Late Cretaceous [*Li et al*., 2007; *Lan et al*., 2008] to a rifting margin by the early Eocene and, during the late early Oligocene, to seafloor spreading and the formation of the South China Sea [*Lin et al*., 2003; *C. Y. Huang et al*., 2012]. The subsequence rift architecture of this part of the Eurasian margin consisted of a broad platform with deep, fault-bounded basins (i.e., the Taishi and Penghu basins, Figure 1) [*Chen and Yang*, 1996; *Hsu et al*., 2001; *Lin et al*., 2005; *Li et al*., 2007; *Lin et al*., 2008; *C. Y. Huang et al*., 2012; *Yeh et al*., 2012] that locally accumulated up to approximately 5 km of clastic sediments [e.g., *Lin et al*., 2003]. To date, little Eocene-age magmatism has been reported from the Taiwan Strait area [e.g., *Yan et al*., 2006] although, recently, *Wang et al*. [2012] and *Huang et al*. [2013] reported Eocene ages from volcanic rocks in the Taiwan Strait and on the island of Taiwan. Extension during the middle and late Miocene affected much of the outer part of the southeast Eurasian margin to various degrees, in particular forming the deep Tainan Basin (TB in Figure 1b) [*Lin et al*., 2003]. The Miocene extension was accompanied by the eruption of voluminous intraplate flood basalts that formed the Penghu Archipelago [*Juang and Chen*, 1992, 1999; *Chung et al*., 1994]. Since the onset of arc-continent collision in Taiwan in the latest Miocene, loading and bending of the Taiwan Strait crust has resulted in the formation of a foreland basin that now contains several kilometers of clastic sediments [*Lin et al*., 2003; *Tensi et al*., 2006].

3. Data and Measurements

In this study, we use the ambient noise surface wave dispersion to investigate the *S* wave velocity structure of the Taiwan Strait. We used the available seismic networks from both side of the strait. These include stations

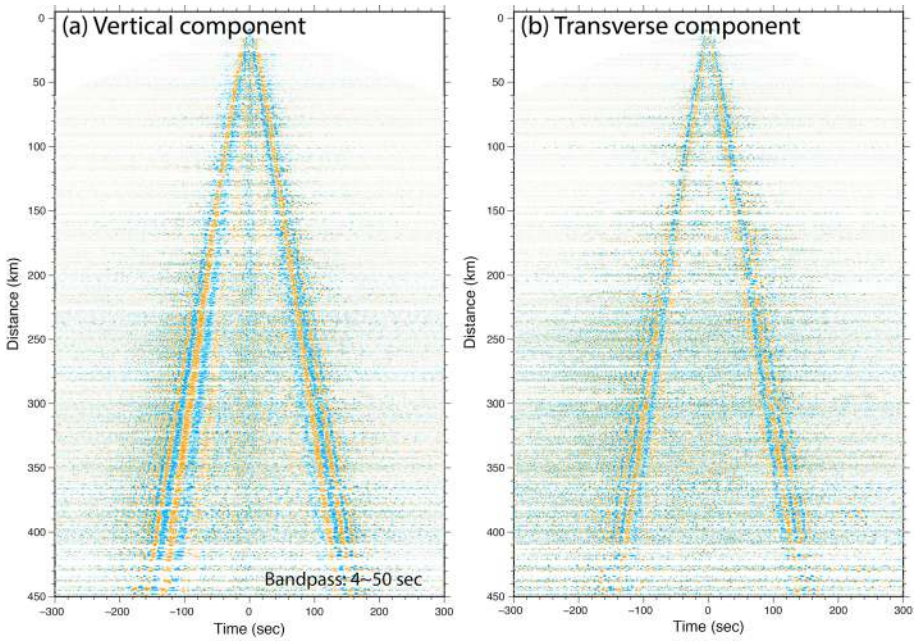

Figure 2. Waveform stacking of CCFs for each station pairs with 4–50 s period band filtered and sorted by interstation distance. (a) Vertical component (EGFs of Rayleigh wave). (b) Transverse component (EGFs of Love wave).

from the Broadband Array in Taiwan for Seismology [*Institute of Earth Sciences, Academia Sinica, Taiwan*, 1996], from the SinoProbe project, and the permanent stations maintained by the Earthquake Administration of Fujian Province (EAFP) (Figure 1a). In total, 45 stations collected continuous three-component data during several time periods; 23 BATS stations that recorded from 2008 to 2013, 16 SinoProbe stations that recorded from 2008 to 2009, and 6 EAFP stations that recorded from 2010 to 2013. The methodology for the data handling can be divided in to four main parts: (1) preparing and organizing the data from each station, (2) extracting the empirical Green's function (EGF) for each station pair by cross correlation, (3) measuring group and phase velocities as a function of frequency for Rayleigh and Love wave dispersion from the EGF, and (4) jointly inverting the dispersion curves to obtain the 3-D *S* wave velocity model. We provide detailed descriptions of each part of the procedure in the following sections.

The data were stored in 1 day periods for each file. For each data period, we removed the daily trends, obtained the mean, and then deconvolved the instrument response. To obtain the surface wave velocity of the fundamental Love wave, the transverse (*T*) component was calculated from two horizontal components that were rotated to radial and transverse components based on the azimuth between the station pair [*Campillo and Paul*, 2003]. The next step consisted in the calculation of the cross-correlation function (CCF) between each pair of stations to represent their corresponding empirical Green's function (EGF) and the CCF in the frequency domain. We also applied spectral whitening to reduce resonance effects at certain frequencies [*Bensen et al*., 2007]. The signal-to-noise ratios of the CCF were enhanced using Welch's method [*Seats et al*., 2012], where the final CCF was derived by stacking the results of the daily records of all CCFs and processing these using a moving window with partial overlap. The windows with anomalous signals (such as earthquakes) were omitted for the CCF calculations by setting a threshold greater than 1.1 times the standard deviation of the amplitude distributions of a particular day (see Figures S1 and S2 in the supporting information for detailed descriptions). Figure 2 shows representative EGFs of each station pair as a function of the interstation distance and EGFs of Rayleigh (Figure 2a) and Love (Figure 2b) waves that display significant dispersion on the waveforms.

In ambient noise formalism, the EGF of a stacked signal at a station pair is approximately coincident with the surface wave Green's function between the two stations (i.e., one station can be thought of as the source and the other as the receiver) and can be treated as such. The vertical and transverse components of the surface waves are dominated by fundamental Rayleigh and Love waves, respectively. We used frequency-time analysis [*Levshin and Lander*, 1989] and an image transformation technique [*Yao et al*., 2005, 2006] to measure

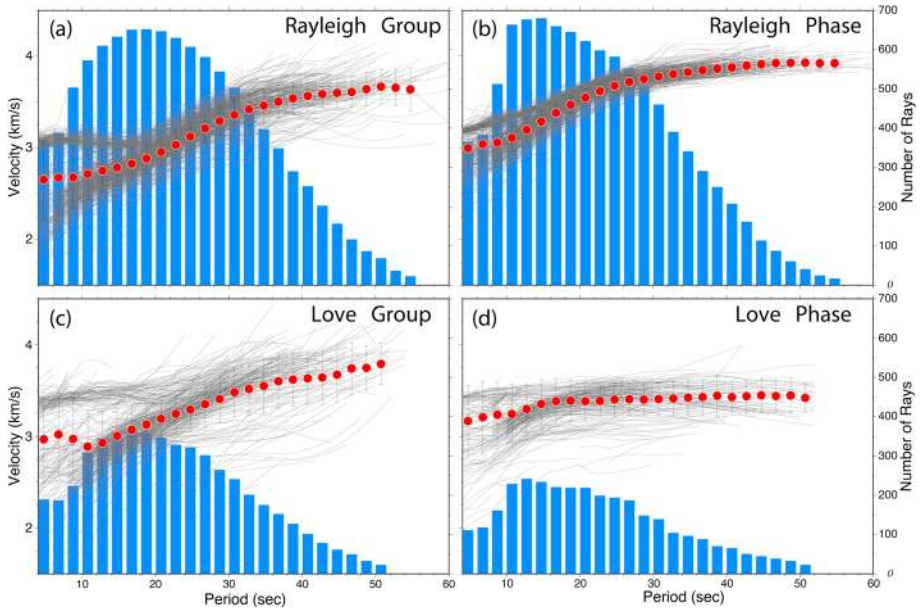

Figure 3. Surface wave velocity measurements at 4 ~ 50 s. (a) Rayleigh wave group velocity. (b) Rayleigh wave phase velocity. (c) Love wave group velocity. (d) Love wave phase velocity. In each panel, black curves represent the dispersion curves as a function of period, while the red dots are the averaged measurements with the associated standard deviation. The number of measurements for each period is shown in the blue histograms.

the EGF group and phase velocities, respectively, as a function of frequency. The frequency-time analysis determines group velocities from the arrival times of the peak of envelopes after applying a Gaussian filter at a different central frequency. The image transformation technique constructs a time period (*t*-*T*) image for the surface wave component. Each column of the image is the normalized amplitude corresponding to the filtered central period (*T*): we used an interval of 2 s for *T* in this study. We then converted the phase velocity (*c*) from time (*t*) by using the far-field representation of the Green's function for the surface wave fundamental mode [*Aki and Richards*, 2002; *Yao et al*., 2006]. The 2π ambiguity of the phase velocity for one period can then be calculated from the previous results of the group velocity. This is based on the assumption that velocity increases with the time period (see Figure S3 in the supporting information for an example of *t*-*T* image). Based on the experience of analyzing the data [*Bensen et al*., 2007; *Lin et al*., 2009; *Porritt et al*., 2011; *Mordret et al*., 2013], the longest measurable period for station pairs depends on its interstation distance, which should be at least 2.5 times larger than the wavelength. Because of this, we measured the dispersion curves over a period ranging from 4 to 50 s (Figure 3). Note that two groups of dispersion curves are clearly visible below 18 s in both the Rayleigh and the Love waves. The high-velocity curves correspond to the ray paths in crystalline rocks in Fujian, while the low-velocity curves can be correlated with sedimentary rocks in the Taiwan Strait (see Figure S4 in the supporting information). Furthermore, the signal-to-noise ratios of the EGF of Love waves are lower than those for Rayleigh waves owing to stronger attenuations of the Love waves [*Shearer*, 2012].

To obtain the 3-D shear velocity structure of the crust, we jointly inverted the Love and Rayleigh phase- and group-dispersion measurements. We applied the wavelet-based sparsity-constrained tomography method described in *Fang et al*. [2015] in which the model parameterization is inherently adaptive to the data distribution. The advantage of this method is that the multiresolution representation of the wavelet transform solves the model parameters (that is, wave speed anomalies) in the wavelet domain, and it resolves features of different scales depending on the strength of the local constraints. In addition, the method deals with ray tracing in an inhomogeneous medium using the fast marching method [*Rawlinson and Sambridge*, 2004]. This results in rays gradually bending toward high-velocity zones. Phase and group velocities are sensitive to changes in the media structure (*Vp*, *Vs*, and density) and, in particular, longer periods are sensitive to deep structure, whereas shorter periods are sensitive to shallower structures. This means that if the model changes at a certain depth, changes will be seen in the dispersion curves at the corresponding periods. The sensitivity kernels strongly depend on the model in which we calculate the partial derivatives. In the first iteration, the *Vs*

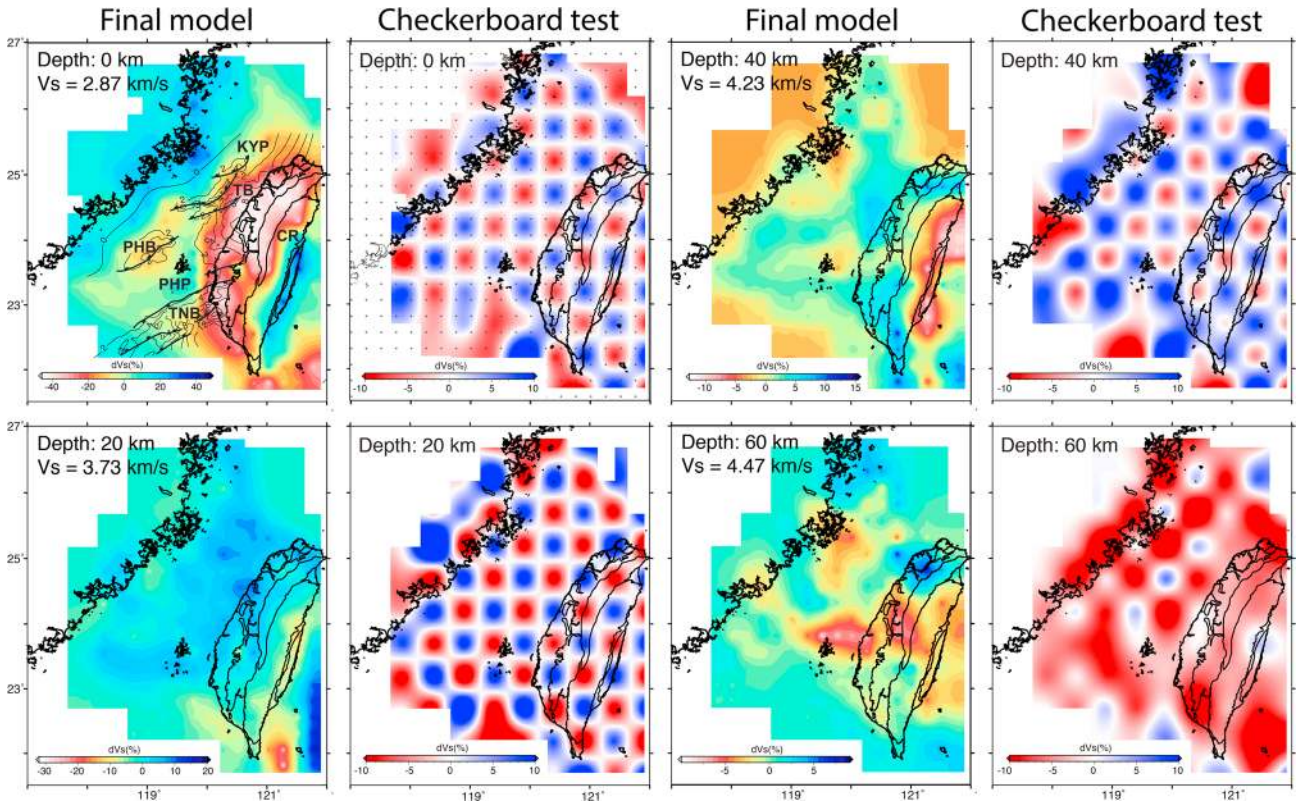

Figure 4. *Vs* velocity perturbation depth slices and the corresponding checkerboard tests at 20 km depth intervals. At 0 km depth, the Cenozoic sediment isopach and normal fault geometries in the Taiwan Strait are from *Lin et al.* [2003].

model is a function of depth, and we scale it to obtain *Vp* and density by using the empirical relationship of *Brocher* [2005]. Although *Vs* accounts for the largest part during the inversion, the sensitivity kernels of both the empirical *Vp* and density are also taken into account in the kernel matrix in the inversion scheme [*Simons and van der Hilst*, 2003; *Fang et al.*, 2015]. After the first iteration, the resultant *Vs* model is taken to be the initial *Vs* model for the next iterations. Also, for each iteration we update the *Vp* and density models from the previous inversion and calculate a new sensitivity kernel and we performed 10 iterations for the final velocity structures (see Figure S5 in the supporting information for the misfit-iteration plot).

4. Resolution Test

In order to test the robustness of the subsurface images, we use two different grid sizes for the inversion: 0.5° (longitude) × 0.5° (latitude) × 5 km (depth) and 0.25° (longitude) × 0.25°(latitude) × 5 km (depth). The large-scale structures from the two grid size inversions are overall similar, although the smaller grid size inversion shows more a detailed structure (see Figures S6 and S7 in the supporting information for the comparison between the path density plots and the results of two grid sizes). The results obtained in the finer grid at shallow depth are consistent with the location and structure of the major basins and platform areas imaged by reflection seismic profiles in the Taiwan Strait [*Lin et al.*, 2003], indicating that these features can be resolved with our data set (Figures 4). Also, the relatively high-velocity zone imaged by our data in Taiwan's Central Range (CR) is consistent with *P* wave tomography results [*Kuo-Chen et al.*, 2012a] and ambient tomography results [*T.-Y. Huang et al.*, 2012] at 0 km depth (Figure 4), furthermore indicating the robustness of our data set for imaging crustal structures. Therefore, taking into consideration the distribution of stations across the Taiwan Strait, we select the inversion results of the smaller grid size (0.25° (longitude) × 0.25° (latitude) × 5 km (depth)) as our preferred model.

In order to assess the resolution of this inversion, we performed checkerboard tests by alternatively assigning 10% positive and negative *S* wave velocity anomalies to adjacent grids using grid sizes 0.5° × 0.5° × 10 km

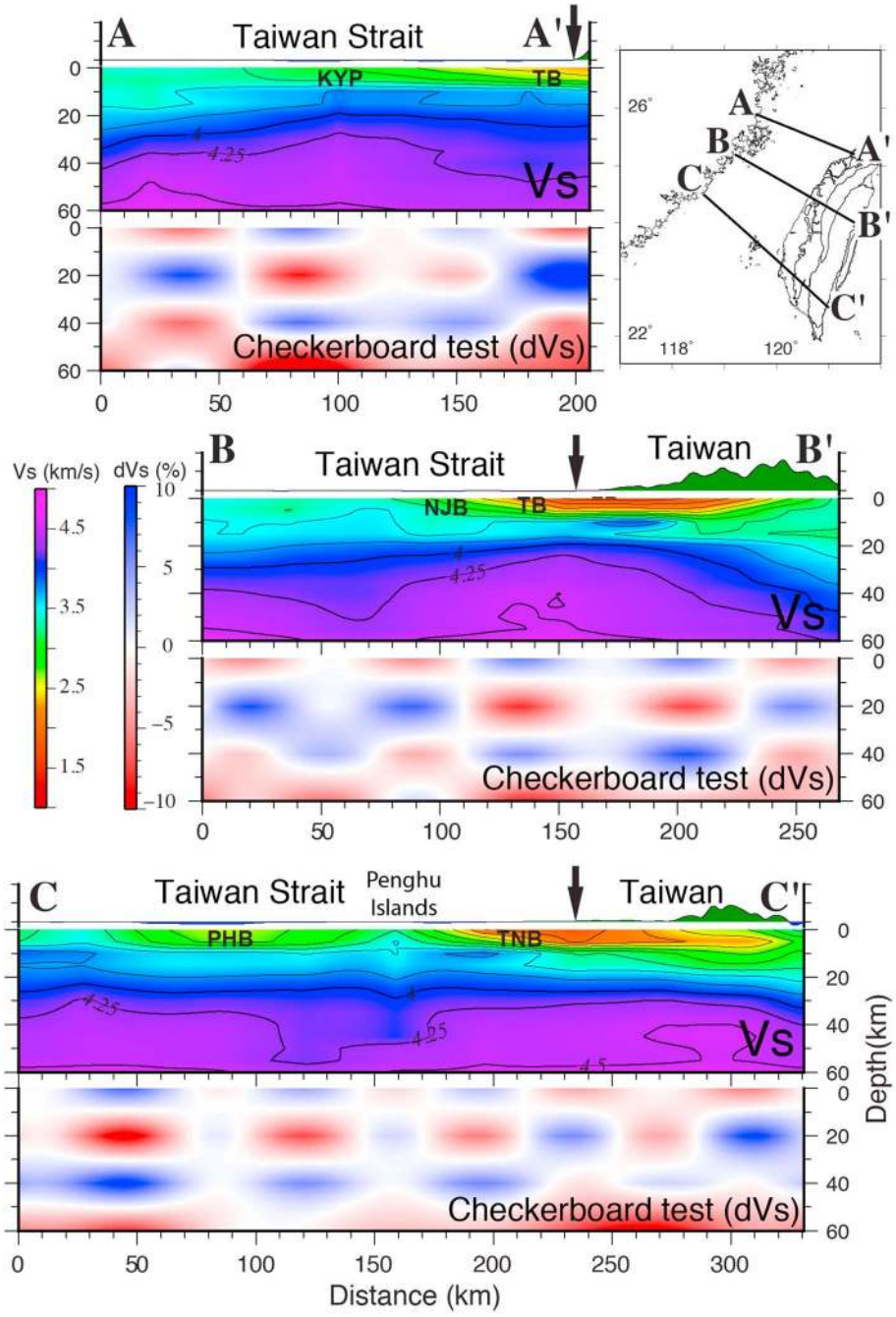

Figure 5. Three vertical sections of the *Vs* model and their checkerboard test. (top right) Location of three sections cross the Taiwan Strait. (top left) *Vs* model and checkerboard test of section AA′. (middle) *Vs* model and checkerboard test of section BB′. (bottom) *Vs* model and checkerboard test of section CC′. NJB: Nanjihtao Basin. TB: Taihsi Basin. PHB: Penghu Basin. TNB: Tainan Basin. KYP: Kuanyin Platform. Thick vertical arrow: the western coastline of Taiwan.

depth in the upper 10 km and 0.5° × 0.5° × 20 km to the base of the model. These checkerboard tests show that from 0 to 40 km depths the crust in the Taiwan Strait and Taiwan are well resolved and from 40 km to 60 km depth can be only roughly resolved for the positive and negative velocity anomalies in the Taiwan Strait. Therefore, on the basis of the resolution test results, we only interpret features with a dimension of ~ 0.5° × 0.5° or larger. Beneath Taiwan, however, the checkerboard test pattern is smeared, indicating that the resolution is poor at this depth range (Figures 4 and 5). Finally, there is a relative low-velocity zone in the lower crust and upper mantle (at 20–60 km depth) beneath the Penghu Archipelago for which we carried out

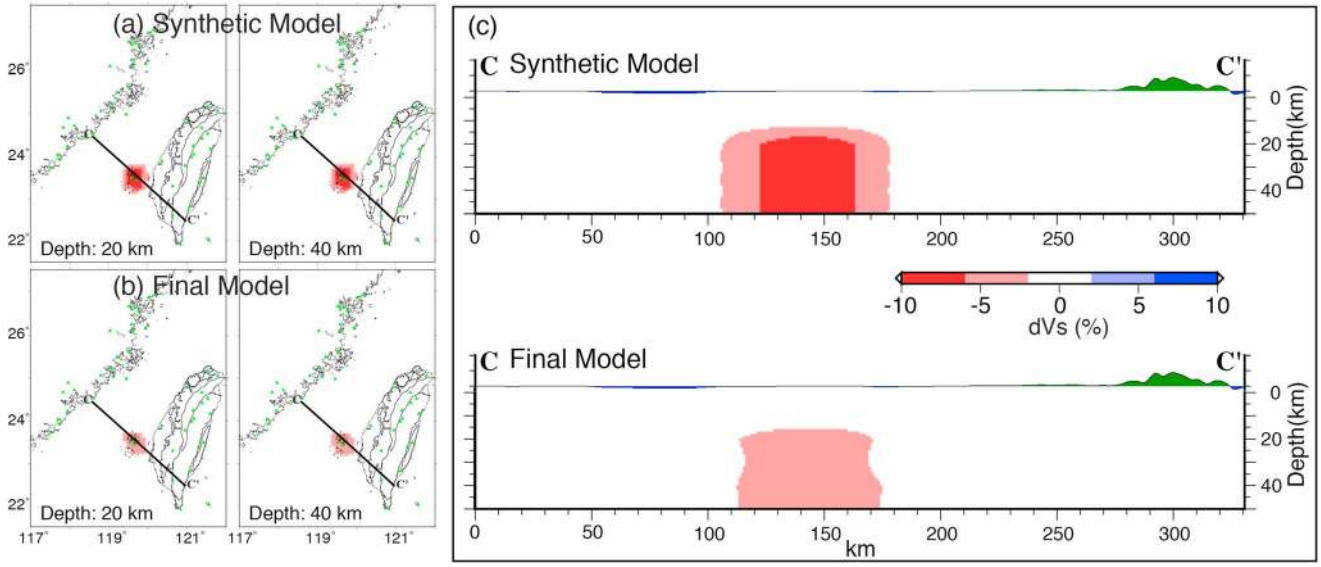

Figure 6. Resolution test of the low-velocity zone beneath the Penghu Archipelago. (a) Map view of the initial model at 20 and 40 depths. (b) Map view of the final model at 20 and 40 km depths. (c) CC′ cross section of the initial and final models.

further tests in order to verify if this result is resolvable with the data set (Figure 6). In this test, raypaths for each station pair were used and the theoretical travel time for each period and for each station pair is calculated based on our input model, which has a lower velocity anomaly beneath Penghu archipelago. We then calculated theoretical travel times as input data to invert the shear velocities in order to see if the low-velocity anomaly is resolvable or not. Technically, the process of the synthetic testing is almost the same as the checkerboard test [*Fang et al*., 2015]. The difference between the two is the input 3-D shear velocity model, which is composed of assigning alternating 10% positive and negative velocity anomalies for the checkerboard test, whereas the synthetic test comprises a local 10% negative velocity anomaly under Penghu archipelago. In the forward calculation, the travel times of Rayleigh and Love waves are calculated for the 3-D input models using the group and phase velocities of each period and for each station pair, respectively. In the inversion, the theoretical travel times serve as the data and a 1-D velocity structure was used as the initial model for the inversion process. The inverted shear wave velocity model is then the result of the checkerboard and synthetic tests in order to see if the velocity anomaly is resolvable or not. The inverted shear wave velocity model results from the synthetic tests suggest that the low-velocity zone beneath the Penghu archipelago can be resolved with this data set (Figure 6).

5. Results

Figure 4 shows map views of the *S* wave velocity perturbation results of our preferred final model and the associated checkerboard tests for depths of 0, 20, 40, and 60 km. At 0 km depth (Figure 4), there is a relative velocity high reaching to 3.5 km/s (Figure 5) along the western side of the Taiwan Strait, near the coastline of China. The rest of the strait displays relative low-velocity zones that coincide with the locations of known major extensional basins imaged by reflection seismic data [*Lin et al*., 2003]. One of these, the Taihsi Basin (TB), displays a velocity of around 2.0 km/s (sections A-A′ and B-B′ of Figure 5) and extends onto the western margin of Taiwan where it coincides with the foreland basin and the uplifted platform sediments in the mountain belt. At 0 km depth, the Penghu Archipelago displays a relatively high velocity (Figure 4) that reaches to about 3.2 km/s (section C-C′ of Figure 5). At 20 km depth, the pattern of velocities is reversed if compared to the 0 km depth image. At this depth, the relatively high-velocity zones along the western side of the Taiwan Strait and in the Penghu Archipelago become relative lows, whereas the areas occupied by the extensional basins become relative velocity highs. This pattern becomes especially well developed at 40 km depth, where the northeastern margin of China and the Penghu Archipelago show strong velocity contrasts compared to the surrounding parts of the margin and the island of Taiwan. This coincides with a pronounced increase of *S* wave velocity to greater than 4.25 km/s beneath the Kuanying Platform and the Taishi Basin

(sections A-A′ and B-B′ of Figure 5), whereas there is a thickening of the crust with a velocity between 4.0 and 4.25 km/s beneath the Penghu Archipelago (section C-C′ of Figure 5). At 60 km depth, the northeastern margin of China and the Penghu Archipelago show pronounced relative velocity lows (Figure 4), with *S* wave velocities of around 4.5 km/s. The velocity structure beneath the island of Taiwan is poorly resolved at this depth.

6. Discussion

The Eurasian continental margin that underlies the Taiwan Strait evolved from a magma-poor rifting margin in the Early Eocene to seafloor spreading and the formation of the South China Sea during the late early Oligocene [*Lin et al*., 2003; *C. Y. Huang et al*., 2012]. In previous studies, the crust below the Taiwan Strait is generally estimated to be about 30 km thick, thickening to greater than 50 km below Taiwan [*Yeh et al*., 1998; *Kim et al*., 2004; *Kuo-Chen et al*., 2012a; *Ustaszewski et al*., 2012; *Huang et al*., 2014; *Wu et al*., 2014]. The determination of sharp discontinuities, such as the Moho, from surface wave dispersion is not straightforward [e.g., *Lebedev et al*., 2013]. In this study, therefore, we estimate the crustal thickness from the calculated *S* wave model by assigning a velocity range of between 4.0 km/s to 4.25 km/s as the crustal-mantle transition (Figure 5). This range of velocity is in agreement with that of *Huang et al*. [2014]. In this way, we estimate the crustal thickness in the western part of the Taiwan Strait to be 30 km ± 2 km, which is similar to that obtained by studies of *Pn* velocity [*Huang et al*., 1998] and gravity data [*Hsieh et al*., 2009]. Beneath the island of Taiwan, however, the crust is thicker than the 40 km depth limit of the model resolution (Figures 5a and 5b), so we cannot make any estimate for the crustal thickness in this area. From northwest to southeast, the crust-mantle transition shows significant topography and velocity anomalies that appear to be related to features developed in the crust (see below).

With the opening of the South China Sea the architecture of the Eurasian margin beneath the Taiwan Strait consisted of a broad platform with deep, northeast-southwest oriented, fault-bounded basins that were subsequently filled with clastic sediments [*Hsu et al*., 2001; *Lin and Watts*, 2002; *Lin et al*., 2003; *Teng and Lin*, 2004; *Cukur et al*., 2011]. In the *Vs* model, the Taihsi and Penghu basins (TB and PHB in Figure 5) are very well imaged as areas with a *S* wave velocity of less than 3 km/s (Figure 5a) and a d*Vs* of around 20% (Figure 7). The extension in depth of these low-velocity anomalies suggests a basins thickness of about 5 km, in agreement with the estimations obtained by *Lin et al*. [2003] from seismic reflection data. In section A-A′ (Figures 5 and 6) a high-velocity zone in the midupper crust beneath the Kuanying Platform (KYP) is associated with a zone of crustal thinning and can be interpreted as intrusive rocks associated with widespread flood volcanism that took place along the margin during the Miocene [e.g., *Juang and Chen*, 1992; *Cukur et al*., 2010]. A similar feature is imaged in sections B-B′ and C-C′ where crustal thinning and a thin, relatively high-velocity zone is present beneath the Taihsi Basin (Figures 5 and 6). We interpret these features to be related to the rifting and Moho uplift that took place during the Eocene. The high-velocity zone imaged in the middle crust beneath the central part of the basin can be interpreted to be a magmatic sill intruded during the rifting, in agreement with recent results from reflection data in East China Sea Basin [*Cukur et al*., 2010].

Extension during the middle and late Miocene affected much of the outer part of the Eurasian margin to various degrees [*Lin et al*., 2003]. This extension was accompanied by the widespread eruption of intraplate flood basalts in the Penghu Archipelago [*Juang and Chen*, 1992, 1999; *Chung et al*., 1994]. Section C-C′ passes through the Penghu Archipelago, imaging a high-velocity anomaly at the surface that extends eastward into the middle crust beneath the western margin of the Tainan Basin (TNB) (Figures 5 and 6). We interpret this feature directly below the Penghu Island as the basaltic edifice built during the lava extrusion. In this scenario of intraplate flood volcanism [e.g., *Huppert and Sparks*, 1988; *Jerram and Widdowson*, 2005], the high-velocity zone beneath the western margin of the Tainan Basin can be interpreted to be a gabbroic sill intruded into the middle crust (Figure 7 section C-C′). Directly below the Penghu archipelago, a low-velocity zone at the base of the crust could be related to the still cooling melt reservoir and magma feeder system that underlies the Penghu volcanic edifice. It is well known that seismic velocities decrease significantly with an increase in temperature [*Christensen and Salibury*, 1979, *Christensen and Mooney*, 1995]. Furthermore, since the duration of heat dissipation in a melt reservoir is the square of the width of the heat-producing zone [*Burg and Gerya*, 2005], the large size of the area of the Penghu Islands at the surface (at least 2500 km^2) suggests that it may take up to 100 Myr to complete the conductive cooling of the entire volcanic plumbing system [*Burg and*

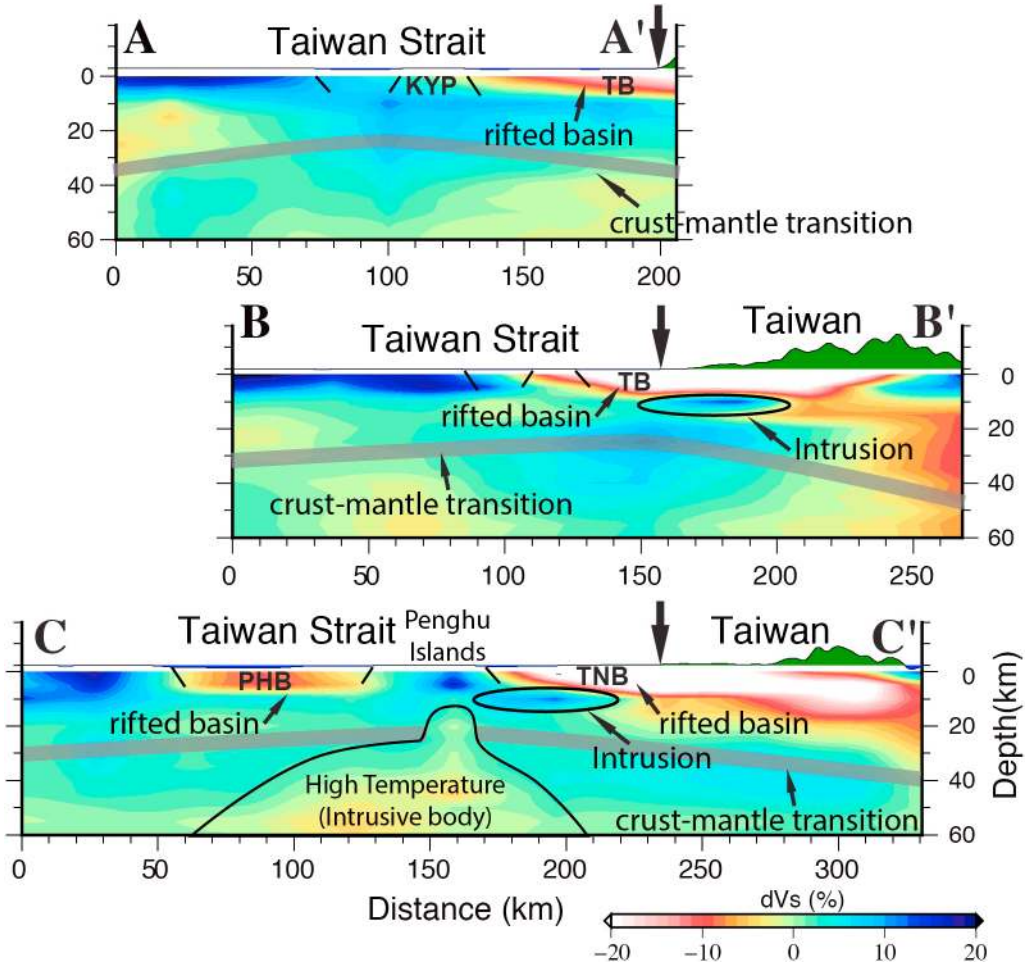

Figure 7. Vertical sections of the shear wave velocity anomalies (d*Vs*) along the profiles showed in Figure 5. Crust-mantle transition is marked by the contours lines between 4 and 4.25 km/s (Figure 5). A low-velocity zone beneath the Penghu Archipelago could relate to a thermal anomaly. TB: Taihsi Basin. PHB: Penghu Basin. TNB: Tainan Basin. KYP: Kuanyin Platform. Thick vertical arrow: the western coastline of Taiwan.

Gerya, 2005]. Therefore, since the volcanic activity in the Penghu Archipelago has been dated at around 16.2 ~ 8.2 Ma [*Juang and Chen*, 1999], elevated temperatures would likely still persist within the crust and upper mantle. Similar low-velocity features thought to be related to high temperature from a lava eruption that occurred 11–12 Myr ago have been imaged in Yellowstone-Snake River Plane [*Roth et al*., 2008].

In sections B-B′ and C-C′ the low-velocity zone that corresponds to the Taihsi Basin (TB in Figure 7), along the west coast of Taiwan (marked by the arrow in Figures 5 and 6), is in part due to sediments being deposited in the foreland basin to the mountain belt [e.g., *Lin and Watts*, 2002; *Tensi et al*., 2006]. This low-velocity zone extends far to the east beneath Taiwan, possibly imaging the accretion of the Taihsi and foreland basin sediments to the orogen's fold and thrust belt. Thickening of the crust in the eastern part of these sections can be attributed to crustal stacking within the mountain belt and to bending of the plate as it enters into the Manila Subduction Zone.

7. Conclusion

In this study, the 3-D crustal structure of the Taiwan Strait has been determined for the first time from a joint Chinese and Taiwanese 3-D ambient noise tomography study. Crustal thickness ranges from 30 km ± 2 km along the coast of China, to about 20 km in the central part of the strait, before increasing to more than 40 km beneath the Taiwan mountain belt (Figure 7). The extensional basins developed in the strait during the Eocene and Miocene are clearly imaged as low-velocity zones that are locally underlain by thin

high-velocity areas interpreted magmatic rocks extruded during the extension. The connection westward between low-velocity zones beneath the island of Taiwan with the Taihsi and the foreland basins suggests that rocks from these basins extend far below the mountain belt. Alternatively, the velocity low beneath the island of Taiwan could, in part, reflect the high heat flow measured there [e.g., *Kuo-Chen et al*., 2012b]. The data also image a high-velocity anomaly near the surface in the Penghu Archipelago that is underlain by a velocity decrease that likely indicates a thermal anomaly related to the still cooling magma reservoir and feeding system to the higher velocity volcanic edifice at the surface. This feature implies that the middle to late Miocene thermal event that produced the Penghu flood basalts still has a significant effect on the crust and upper mantle in this part of the Taiwan Strait.

Acknowledgments

H.K-C. is supported by Ministry of Science and Technology (grant MOST 104-2628-M-008-005-MY3). D. Brown acknowledges funding by MINECO grant CGL2013-43877-P. Q. Li and Z. Ye acknowledge funding by Sinoprobe-02-03. *S* wave tomography model presented in all figures can be obtained from the lead author (Hao Kuo-Chen, kuochen@ncu.edu.tw). Discussion with F. Wu of Binghamton University and W. L. Chang of National Central University is highly appreciated.

References

Aki, K., and P. G. Richards (2002), *Quantitative Seismology*, Univ. Sci. Books, Sausalito, Calif.

Bensen, G. D., M. H. Ritzwoller, M. P. Barmin, A. L. Levshin, F. Lin, M. P. Moschetti, N. M. Shapiro, and Y. Yang (2007), Processing seismic ambient noise data to obtain reliable broad-band surface wave dispersion measurements, *Geophys. J. Int.*, *169*, 1239–1260, doi:10.1111/j.1365-246X.2007.03374.x.

Brocher, T. M. (2005), Empirical relations between elastic wavespeeds and density in the Earth's crust, *Bull. Geol. Soc. Am.*, *95*(6), 2081–2092, doi:10.1785/0120050077.

Burg, J. P., and T. V. Gerya (2005), The role of viscous heating in Barrovian metamorphism of collisional orogens: Thermomechanical models and application to the Lepontine Dome in the Central Alps, *J. Metamorph. Geol.*, *23*, 75–95, doi:10.1111/j.1525-1314.2005.00563.x.

Campillo, M., and A. Paul (2003), Long-range correlations in the diffuse seismic coda, *Science*, *299*, 547–549, doi:10.1126/science.1078551.

Chen, A. T., and Y. L. Yang (1996), Lack of compressional overprint on the extensional structure in offshore Tainan and the tectonic implications, *Terr. Atmos. Ocean. Sci.*, *4*, 505–522.

Christensen, N. I., and W. D. Mooney (1995), Seismic velocity structure and composition of the continental crust—A global view, *J. Geophys. Res.*, *100*, 9761–9788, doi:10.1029/95JB00259.

Christensen, N. I., and M. H. Salisbury (1979), Seismic anisotropy in the oceanic upper mantle: Evidence from the Bay of Islands Ophiolite Complex, *J. Geophys. Res.*, *84*, 4601–4610, doi:10.1029/JB084iB09p04601.

Chung, S. L., S. S. Sun, K. Tu, C. H. Chen, and C. Y. Lee (1994), Late Cenozoic basaltic volcanism around the Taiwan Strait, SE China: Product of lithosphere–asthenosphere interaction during continental extension, *Chem. Geol.*, *112*, 1–20.

Cukur, D., S. Horozal, D. C. Kim, G. H. Lee, C. H. Han, and M. H. Kang (2010), The distribution and characteristics of the igneous complexes in the northern East China Sea Shelf Basin and their implications for hydrocarbon potential, *Mar. Geophys. Res.*, *31*(4), 299–313, doi:10.1007/s11001-010-9112-y.

Cukur, D., S. Horozal, D. C. Kim, and H. C. Han (2011), Seismic stratigraphy and structural analysis of the northern East China Sea Shelf Basin interpreted from multi-channel seismic reflection data and cross-section restoration, *Mar. Pet. Geol.*, *28*, 1003–1022, doi:10.1016/j.marpetgeo.2011.01.002.

Fang, H., H. Yao, H. Zhang, Y. C. Huang, and R. D. Van Der Hilst (2015), Direct inversion of surface wave dispersion for 3-D shallow crustal structure based on ray tracing: Methodology and application, *Geophys. J. Int.*, *201*, 1251–1263, doi:10.1093/gji/ggv080.

Franke, D. (2013), Rifting, lithosphere breakup and volcanism: Comparison of magma-poor and volcanic rifted margins, *Mar. Pet. Geol.*, *43*, 63–87, doi:10.1016/j.marpetgeo.2012.11.003.

Gao, T., and H. Huang (1994), Tectonic characteristics and evolution of the Taiwan Strait, *Acta Geol. Sin.*, *68*(3), 197–207, doi:10.1111/j.1755-6724.1995.mp8001001.x.

Hsieh, H. H., H. Y. Yen, and M. H. Shih (2009), Moho depth derived from gravity data in the Taiwan Strait area, *Terr. Atmos. Ocean Sci.*, *2*, 235–241, doi:10.3319/TAO.2009.03.05.01(T).

Hsu, S. K., J. C. Sibuet, and C. T. Shyu (2001), Magnetic inversion in the East China Sea and Okinawa Trough: Tectonic implications, *Tectonophysics*, *333*, 111–122, doi:10.1016/S0040-1951(00)00270-5.

Huang, B. S., K. C. Chen, K. L. Wang, and H. Y. Yen (1998), Velocities of *Pn*-waves in the Taiwan strait and its surrounding area from regional earthquakes, *Terr. Atmos. Ocean Sci.*, *9*, 473–486.

Huang, C. Y., Y. Yin, Q. H. Zhao, and C. T. Lin (2012), Cenozoic stratigraphy of Taiwan: Window into rifting, stratigraphy and paleoceanography of South China Sea, *Chin. Sci. Bull.*, *57*, 3130–3149, doi:10.1007/s11434-012-5349-y.

Huang, C. Y., W. R. Chi, Y. Yan, K. M. Yang, P. M. Liew, M. S. Wu, J. C. Wu, and C. Zhang (2013), The first record of Eocene tuff in a Paleogene rift basin near Nantou, Western Foothills, central Taiwan, *J. Asian. Earth Sci.*, *69*, 3–16, doi:10.1016/j.jseaes.2013.02.022.

Huang, T.-Y., Y. Gung, W.-T. Liang, L.-Y. Chiao, and L. S. Teng (2012), Broad-band Rayleigh wave tomography of Taiwan and its implications on gravity anomalies, *Geophys. Res. Lett.*, *39*, L05305, doi:10.1029/2011GL050727.

Huang, Y. C., H. Yao, F. T. Wu, W. T. Liang, B. S. Huang, C. H. Lin, and K. L. Wen (2014), Crustal and upper mantle *S*-wave velocity structures across the Taiwan Strait from ambient seismic noise and teleseismic Rayleigh wave analyses, *J. Asian Earth Sci.*, *81*, 38–52, doi:10.1016/j.jseaes.2013.11.023.

Huppert, H. E., and S. J. Sparks (1988), The generation of granitic magmas by intrusion of basalt into continental crust, *J. Petrol.*, *29*, 599–624.

Institute of Earth Sciences, Academia Sinica, Taiwan (1996), Broadband Array in Taiwan for Seismology, Institute of Earth Sciences, Academia Sinica, Taiwan. Other/Seismic Network, doi:10.7914/SN/TW.

Jerram, D. A., and M. Widdowson (2005), The anatomy of continental flood basalt provinces: Geological constraints on the processes and products of flood volcanism, *Lithos*, *79*, 385–405, doi:10.1016/j.lithos.2004.09.009.

Juang, W. S., and J. C. Chen (1992), Geochronology and geochemistry of Penghu basalts, Taiwan Strait and their tectonic significance, *J. Southeast Asian Earth Sci.*, *2/3*, 185–193.

Juang, W.-S., and J.-C. Chen (1999), The nature and origin of Penghu basalts: A review, *Bull. Central Geol. Surv.*, *12*, 147–200.

Kim, K. H., J. M. Chiu, H. Kao, Q. Liu, and Y. H. Yeh (2004), A preliminary study of crustal structure in Taiwan region using receiver function analysis, *Geophys. J. Int.*, *159*, 146–164, doi:10.1111/j.1365-246X.2004.02344.x.

Kuo, Y. W., et al. (2015), Crustal structures from the Wuyi-Yunkai orogen to the Taiwan orogen: The onshore-offshore wide-angle seismic experiments of the TAIGER and ATSEE projects, *Tectonophysics*, doi:10.1016/j.tecto.2015.09.014.

Kuo-Chen, H., F. T. Wu, and S. W. Roecker (2012a), Three-dimensional *P* velocity structures of the lithosphere beneath Taiwan from the analysis of TAIGER and related seismic data sets, *J. Geophys. Res.*, *117*, B06306, doi:10.1029/2011JB009108.
Kuo-Chen, H., F. Wu, D. M. Jenkins, J. Mechie, S. Roecker, C.-Y. Wang, and B.-S. Huang (2012b), Seismic evidence for the α-β quartz transition beneath Taiwan from *Vp/Vs* tomography, *Geophys. Res. Lett.*, L22302, doi:10.1029/2012GL053649.
Lan, C. Y., C. S. Lee, T. F. Yui, H. T. Chu, and B. M. Jahn (2008), The tectono-thermal events of Taiwan and their relationship with SE China, *Terr. Atmos. Ocean. Sci.*, *19*, 257–278, doi:10.3319/TAO.2008.19.3.257(TT).
Lebedev, S., J. Adam, and T. Meier (2013), Mapping the Moho with seismic surface waves: A review, resolution analysis, and recommended inversion strategies, *Tectonophysics*, *609*, 377–394, doi:10.1016/j.tecto.2012.12.030.
Levshin, A. L., and A. V. Lander (1989), Recording, identification and measurement of surface wave parameters, in *Seismic Surface Waves in a Laterally Inhomogeneous Earth*, edited by V. I. Keilis-Borok, pp. 131–182, Kluwer Acad., Dordrecht, Netherlands.
Li, C. F., Z. Zhou, J. Li, H. Hao, and J. Geng (2007), Structures of the northeasternmost South China Sea continental margin and ocean basin: Geophysical constraints and tectonic implications, *Mar. Geophys. Res.*, *28*, 59–79, doi:10.1007/s11001-007-9014-9.
Lin, A. T., and A. B. Watts (2002), Origin of the West Taiwan basin by orogenic loading and flexure of a rifted continental margin, *J. Geophys. Res.*, *107*(B9), 2185, doi:10.1029/2001JB000669.
Lin, A. T., A. B. Watts, and S. P. Hesselbo (2003), Cenozoic stratigraphy and subsidence history of the South China Sea margin in the Taiwan region, *Basin Res.*, *15*, 453–478, doi:10.1046/j.1365-2117.2003.00215.
Lin, A. T., C. S. Liu, C. C. Lin, P. Schnurle, G. Y. Chen, W. Z. Liao, L. S. Teng, H. J. Chuang, and M. S. Wu (2008), Tectonic features associated with the overriding of an accretionary wedge on top of a rifted continental margin: An example from Taiwan, *Mar. Geol.*, *255*, 186–203, doi:10.1016/j.margeo.2008.10.002.
Lin, F.-C., M. H. Ritzwoller, and R. Sneider (2009), Eikonal tomography: Surface wave tomography by phase front tracking across a regional broadband seismic array, *Geophys. J. Int.*, *177*, 1091–1110.
Lin, J. Y., J. C. Sibuet, and S. K. Hsu (2005), Distribution of the East China Sea continental shelf basins and depths of magnetic sources, *Earth Planets Space*, *57*, 1063–1072, doi:10.1186/BF03351885.
Mordret, A., N. M. Shapiro, S. Singh, P. Roux, and O. I. Barkved (2013), Helmholtz tomography of ambient noise surface wave data to estimate Scholte wave phase velocity at Valhall life of the field, *Geophysics*, *78*(2), WA99–WA109.
Mouthereau, F., and C. Petit (2003), Rheology and strength of the Eurasian continental lithosphere in the foreland of the Taiwan collision belt: Constraints from seismicity, flexure, and structural styles, *J. Geophys. Res.*, *108*(B11), 2512, doi:10.1029/2002JB002098.
Porritt, R. W., R. M. Allen, D. C. Boyarko, and M. R. Brudzinski (2011), Investigation of Cascadia segmentation with ambient noise tomography, *Earth Planet. Sci. Lett.*, *309*(1), 67–76.
Rawlinson, N., and M. Sambridge (2004), Wavefront evolution in strongly heterogeneous layered media using the fast marching method, *Geophys. J. Int.*, *156*, 631–647, doi:10.1111/j.1365-246X.2004.02153.x.
Roth, J. B., M. J. Fouch, D. E. James, and R. W. Carlson (2008), Three-dimensional seismic velocity structure of the northwestern United States, *Geophy. Res. Lett.*, *35*, L15304, doi:10.1029/2008GL034669.
Seats, K. J., J. F. Lawrence, and G. A. Prieto (2012), Improved ambient noise correlation functions using Welch's method, *Geophys. J. Int.*, *188*, 513–523, doi:10.1111/229j.1365-246X.2011.05263.x.
Shearer, P. M. (2012), *Introduction to Seismology*, 2nd ed., Cambridge Univ. Press, Cambridge.
Sibuet, J. C., and S. K. Hsu (1997), Geodynamics of the Taiwan arc-arc collision, *Tectonophysics*, *274*, 221–251, doi:10.1016/S0040-1951(96)00305-8.
Sibuet, J. C., and S. K. Hsu (2004), How was Taiwan created? *Tectonophysics*, *379*, 159–181, doi:10.1016/j.tecto.2003.10.022.
Simons, F. J., and R. D. van der Hilst (2003), Seismic and mechanical anisotropy and the past and present deformation of the Australian lithosphere, *Earth Planet. Sci. Lett.*, *211*, 271–286.
Suppe, J. (1984), Kinematics of arc-continent collision, flipping of subduction and back-arc spreading near Taiwan, *Mem. Geol. Soc. China*, *6*, 21–33.
Teng, L. S., and A. T. Lin (2004), Cenozoic tectonics of the China continental margin: Insights from Taiwan, in *Aspects of the Tectonic Evolution of China*, *Geol. Soc. London Spec. Publ.*, *226*, pp. 313–332, doi:10.1144/GSL.SP.2004.226.01.17.
Tensi, J., F. Mouthereau, and O. Lacombe (2006), Lithospheric bulge in the West Taiwan Basin, *Basin Res.*, *18*(3), 277–299, doi:10.1111/j.1365-2117.2006.00296.x.
Ustaszewski, K., Y. M. Wu, J. Suppe, H. H. Huang, C. H. Chang, and S. Carena (2012), Crust-mantle boundaries in the Taiwan - Luzon arc-continent collision system determined from local earthquake tomography and 1D models: Implications for the mode of subduction polarity reversal, *Tectonophysics*, *578*, 31–49, doi:10.1016/j.tecto.2011.12.029.
Wang, K. L., S. L. Chung, Y. M. Lo, C. H. Lo, H. J. Yang, R. Shinjo, T. Y. Lee, J. C. Wu, and S. T. Huang (2012), Age and geochemical characteristics of Paleogene basalts drilled from western Taiwan: Records of initial rifting at the southeastern Eurasian continental margin, *Lithos*, *155*, 426–441, doi:10.1016/j.lithos.2012.10.002.
Wu, F. T., H. Kuo-Chen, and K. McIntosh (2014), Subsurface imaging, TAIGER experiments and tectonic models of Taiwan, *J. Asian Earth Sci.*, *90*, 173–208, doi:10.1016/j.jseaes.2014.03.024.
Yan, P., H. Deng, H. Liu, Z. Zhang, and Y. Jiang (2006), The temporal and spatial distribution of volcanism in the South China Sea region, *J. Asian Earth Sci.*, *27*, 647–659, doi:10.1016/j.jseaes.2005.06.005.
Yao, H., G. Xu, L. Zhu, and X. Xiao (2005), Mantle structure from inter-station Rayleigh wave dispersion and its tectonic implication in Western China and neighboring regions, *Phys. Earth Planet. Inter.*, *148*, 39–54, doi:10.1016/j.pepi.2004.08.006.
Yao, H., R. D. van der Hilst, and M. V. de Hoop (2006), Surface-wave array tomography in SE Tibet from ambient seismic noise and two-station analysis: I—Phase velocity maps, *Geophys. J. Int.*, *166*, 732–744, doi:10.1111/j.1365-246X.2006.03028.x.
Yeh, Y. C., S. K. Hsu, W. B. Doo, J. C. Sibuet, C. S. Liu, and C. S. Lee (2012), Crustal features of the northeastern South China Sea: Insights from seismic and magnetic interpretations, *Mar. Geophys. Res.*, *33*, 307–326, doi:10.1007/s11001-012-9154-4.
Yeh, Y. H., et al. (1998), Onshore/offshore wide-angle deep seismic profiling in Taiwan, *Terr. Atmos. Ocean. Sci.*, *9*, 301–316.